Journal of Power Sources 195 (2010) 7787–7795

Contents lists available at ScienceDirect

Journal of Power Sources

journal homepage: www.elsevier.com/locate/jpowsour

Three-dimensional thermo-fluid and electrochemical modeling of anode-supported planar solid oxide fuel cell

Zuopeng Qu[a,*], P.V. Aravind[a], N.J.J. Dekker[b], A.H.H. Janssen[b], N. Woudstra[a], A.H.M. Verkooijen[a]

[a] Department of Process & Energy, Delft University of Technology, The Netherlands
[b] Energy research Centre of the Netherlands (ECN), The Netherlands

ARTICLE INFO

Article history:
Received 2 November 2009
Received in revised form 2 February 2010
Accepted 7 February 2010
Available online 24 February 2010

Keywords:
Three-dimensional
Solid oxide fuel cell
CFD modeling
Radiation

ABSTRACT

This paper presents a three-dimensional model of an anode-supported planar solid oxide fuel cell with corrugated bipolar plates serving as gas channels and current collector above the active area of the cell. Conservation equations of mass, momentum, energy and species are solved incorporating the electrochemical reactions. Heat transfer due to conduction, convection and radiation is included. An empirical equation for cell resistance with measured values for different parameters is used for the calculations. Distribution of temperature and gas concentrations in the PEN (positive electrode/electrolyte/negative electrode) structure and gas channels are investigated. Variation of current density over the cell is studied. Furthermore, the effect of radiation on the temperature distribution is studied and discussed. Modeling results show that the relatively uniform current density is achieved at given conditions for the proposed design and the inclusion of thermal radiation is required for accurate prediction of temperature field in the single cell unit.

1. Introduction

Fuel cells are energy conversion devices which can produce electricity and heat (such as high temperature fuel cell, SOFC) directly from a gaseous or gasified fuel by electrochemical reaction of that fuel with an oxidant. Because of the high efficiency and low emission level of pollutants fuel cells are considered to be an environment-friendly way of producing electricity. Furthermore, with the increasingly visible multi-fuel capability, solid oxide fuel cells are being paid more attention recently [1].

However, the development of SOFC is still facing some challenging problems, such as proven longer life time, a lower net cost and an elevated performance, towards its large-scale commercialization and profitability [2]. In order to achieve these, a better detailed understanding of the internal processes and an accurate prediction of operating parameters inside the fuel cell is required. The SOFC's high operating temperature makes the experimental investigation and measurement of these parameters costly and difficult, therefore mathematical modeling becomes an important tool to evaluate the performance, identify and overcome the problems faced by the development of SOFCs.

Among all these parameters, the accurate determination of the temperature distribution is of particular significance because the majority of the decisive parameters governing the performance of fuel cells, for instance, material properties, chemical kinetics and current densities, etc., are heavily depending on the temperatures. In addition to these, to avoid the mechanical failure of cell structure, temperature gradients are required to calculate the thermal stress in the cell. Therefore, a number of theoretical models have been developed to predict the temperature profile of SOFC. Studies of one-, two- or three-dimensional models with various configurations and geometries have been published for either tubular or planar types of SOFCs [3–15].

However, most of the models so far reported have the deficiencies in either simply ignoring the electrochemical reaction happening in the fuel cell [3], or assuming reactions taking place in the gas phase or surface area instead of the solid-phase volumetric reactions [4]. Some models only consider the cell as a single solid-phase and neglect the effect of the diffusion of gases through the porous electrodes [5]. The resistance used in the electrochemical model is calculated theoretically rather than experimentally [6]. Additionally, for simplicities the effect of thermal radiation is not taken into account in predicting the temperature of fuel cell [7]. The limitations of these models may affect the accuracy and reliability of the results [8].

In this study, a three-dimensional thermo-fluid model coupled with electrochemical reaction for an anode-supported planar SOFC has been developed to investigate the internal processes and temperature distribution within a single cell unit for the proposed design. The electrochemical reactions, heat and mass

* Corresponding author. Tel.: +31 015 278 3688; fax: +31 015 278 2460.
E-mail address: z.qu@tudelft.nl (Z. Qu).

0378-7753/$ – see front matter © 2010 Elsevier B.V. All rights reserved.
doi:10.1016/j.jpowsour.2010.02.016

Nomenclature

C	molar concentration
C_p	heat capacity at constant pressure
D	diffusion coefficient
E_a	activation energy
F	Faraday constant
g	Gibbs free energy
h	enthalpy
H	height
i	current density
k	conductive heat transfer coefficient
L	cell length
M	molar mass
n	no. of moles
N	molar flux
R	universal gas constant
r	reaction rate
S	source
t	time
T	temperature
v	velocity
V	voltage
Vj	Fuller diffusion volume
W	cell unit width
X	concentration
Y	mass fraction

Greek

α	permeability
α_r	absorption coefficient
ρ	density
λ	thermal conductivity
γ	porosity
μ	viscosity
η	potential (voltage) drop
τ	thickness

Subscripts

a	anode
act	activation
atm	atmospheric
c	cathode
e	electrolyte
ECR	electrochemical reaction
eff	effective
f	fuel
fl	fluid
i	species i
ic	interconnect
inlet	inlet of the gas channel
loc	local
M	momentum
ohm	ohmic
rev	reversible
s	solid
tot	total

Superscripts

0	reference
reac	reacted

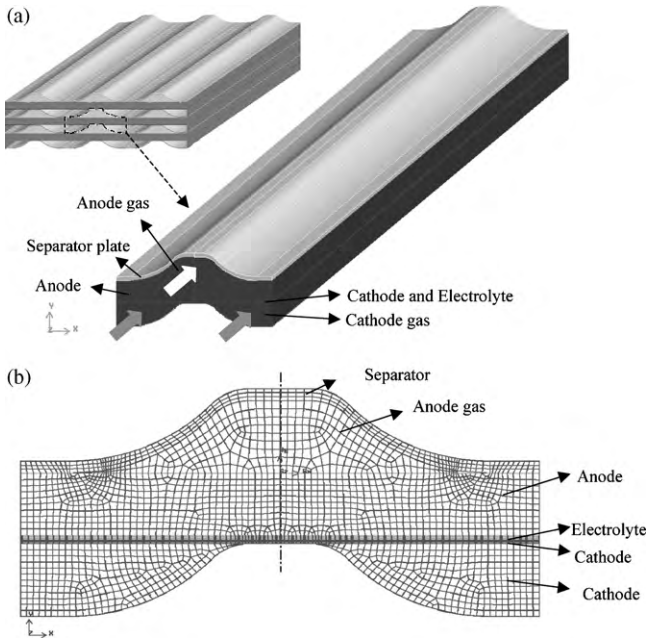

Fig. 1. Geometric model: (a) three-dimensional view of the modeled one single channel unit in the cell (b) the front view of the channels with grids.

transfer phenomena between the solid and gas phases have all been included in the cell model. The conservation equations are solved by using commercial computational fluid dynamics (CFD) software Fluent and the coupled electrochemical processes are simulated by external user-defined subroutines. The electrochemical model utilizes a simple equation for the cell resistance with experimentally determined values of the different parameters for calculating the electrochemical parameters. The variation of gaseous species concentrations, distribution of current density and temperature profile, etc., over the cell unit are presented and discussed. Furthermore, the effects of thermal radiation are investigated by comparison between the cases with and without radiation heat transfer.

2. SOFC model development

2.1. Model specifications

The geometric model studied in this work is shown in Fig. 1. The proposed configuration is based on the design of anode-supported planar SOFC with corrugated bipolar plates serving as gas channels and current collector above and below the active area of the cell. The model developed in this work considers a single cell unit representing a repeated unit in the stack. The simulation of the single cell unit is supposed to be representative for the behavior of the whole stack, except the channels at the edges of the stack where boundary conditions and active cell area could be different. As shown in Fig. 1a the present model is based on the co-flow design, in which anode gas and cathode gas flows on both sides of the cell in the same direction. Fig. 1b shows the cross-section of the single cell unit and resulting grids for the calculation. The mesh is locally refined at the regions where the geometry changes dramatically. The cell is in the middle of the corrugated plates. The fuel gas channel is between the anode and the corrugated separator plate and on the other side the corresponding air channel is located between the cathode and separator plate. The specifications and some input data of the present model are summarized in Table 1.

Table 1
Model specifications and input parameters.

	Specifications	Input data
Geometric parameters	Anode thickness (τ_a)	0.55 mm
	Cathode thickness (τ_c)	0.03 mm
	Electrode thickness (τ_e)	0.01 mm
	Interconnect thickness (τ_{ic})	0.2 mm
	Cell length (L)	112 mm
	Unit channel width (W)	4 mm
	Fuel channel height (H_f)	0.6 mm
	Air channel height (H_a)	0.6 mm
Material properties	Anode density (ρ_a)	7740 kg m^{-3}
	Anode thermal conductivity (λ_a)	6 W m^{-1} K^{-1}
	Anode heat capacity ($C_{p,a}$)	0.6 kJ kg^{-1} K^{-1}
	Anode porosity (γ)	30%
	Cathode density (ρ_c)	5300 kg m^{-3}
	Cathode thermal conductivity (λ_c)	10 W m^{-1} K^{-1}
	Cathode heat capacity ($C_{p,c}$)	0.607 kJ kg^{-1} K^{-1}
	Cathode porosity (γ)	30%
	Electrolyte density (ρ_e)	6000 kg m^{-3}
	Electrolyte thermal conductivity (λ_e)	2.7 W m^{-1} K^{-1}
	Electrolyte heat capacity ($C_{p,e}$)	0.4 kJ kg^{-1} K^{-1}
	Interconnect density (ρ_{ic})	2719 kg m^{-3}
	Interconnect thermal conductivity (λ_{ic})	202.4 W m^{-1} K^{-1}
	Interconnect heat capacity ($C_{p,ic}$)	0.871 kJ kg^{-1} K^{-1}
Operating parameters	Pressure (P)	1 bar
	Fuel inlet temperature ($T_{f,inlet}$)	973 K
	Air inlet temperature ($T_{a,inlet}$)	973 K
	Top and bottom external walls	Adiabatic
	Operating voltage (V_{cell})	0.8 V
	Fuel feed	95% H_2, 5% H_2O
	Air feed	21% O_2, 79% N_2
	Air to fuel ratio	10
	Fuel utilization (U_{fuel})	0.8
Electrochemical parameters	Activation energy (E_a)	−101,248 J mol^{-1} K^{-1}
	Empirical parameter (k_0)	1.8870e^{-10} ohm m^2
	Faraday constant (F)	96,485 C mole $^{-1}$
	Universal gas constant (R)	8.314 J mole^{-1} K^{-1}

2.2. Thermo-fluid model

In this three-dimensional CFD modeling work, the solid and fluid (including porous part) domains are divided into many discrete meshes, shown in Fig. 1b. In each computational grid, the following conservation equations of mass, momentum, species and energy are solved by finite volume method.

$$\nabla(\rho\vec{v}) = S_{\text{mass}} \tag{1}$$

$$\nabla(\rho\vec{v}\vec{v}) + \nabla p - \nabla\left[\mu(\nabla\vec{v} + \nabla\vec{v}^T) - \frac{2\mu}{3}\nabla\vec{v}I\right] = S_M \tag{2}$$

The conservation equations of mass and momentum are shown in Eqs. (1) and (2), respectively, where S_{mass} is the mass source added to the continuous phase using user-defined sources. In order to simplify the model, the current modeling work treats the whole anode and cathode substrates as the porous media with same properties. However, in the model the reaction region, the active anode thin layers, was distinguished from the thick support anode by specifying the reaction zone inside anode. For simplification the reaction zone is at the interface between the anode and electrolyte. The additional momentum source caused by the porous media in the model is contained in the term S_M. The flow velocity of gases in the porous electrodes is low and can be considered as laminar flow. In case of laminar flows through porous media, the additional momentum source caused by the porous media in the model can be simplified as Darcy's law (3):

$$\nabla p = -\frac{\mu}{\alpha}\vec{v} \tag{3}$$

Generally, the gas species transfer mainly by convection in the flow channels and diffusion in the porous electrodes. The species conservation can be expressed in Eq. (4):

$$\nabla(\rho\vec{v}Y_i) = \nabla\left(\sum_{j=1}^{n-1}\rho D_{ij}\nabla Y_j\right) + S_i \tag{4}$$

where S_i are the species sources in the model, which include the net rate of the production of species i (H_2, O_2, H_2O, N_2) and the rate of the additional creation from user-defined sources. D_{ij} is the binary diffusion coefficient. In the porous solid structure of electrodes the gases have to diffuse through the pores of porous anode or cathode to reach the reaction site, where the diffusion-dominated laminar gas flows involve various chemical species.

The Fuller method based on the kinetic theory diffusion coefficient equation is utilized for the calculation of the binary diffusion coefficients D_{ij}. With two gases present at the cathode side and two gases at the anode side there are totally two possible binary diffusion coefficients. The Fuller et al. expression for the binary diffusion coefficient of a mixture of two gases i and j is shown in Eqs. (5) and (6) [16,17].

$$D_{ij} = \frac{0.00143T^{1.75}}{PM_{ij}^{1/2}\left(V_i^{1/3} + V_j^{1/3}\right)^2} \tag{5}$$

$$M_{ij} = 2\left(M_i^{-1} + M_j^{-1}\right)^{-1} \tag{6}$$

Tables 2 and 3 illustrate the special Fuller et al. diffusion volume (V_i) and binary diffusion coefficients (D_{ij}) used in the modeling, respectively.

For the mass balance in the model, the chemical species of H_2O, H_2 and O_2 are considered at the anode side and O_2 and N_2 are at

Table 2
The special Fuller et al. diffusion volume.

	H_2O	H_2	N_2	O_2
Fuller diffusion volume	13.1	6.12	18.5	16.3

Table 3
Binary diffusion coefficients.

i	j	M_{ij}	$D_{ij}/T^{1.75}$
H_2	H_2O	3.626113	1.9562E−5
O_2	N_2	29.87377	3.4549E−6

the cathode side. The electrochemical reaction of hydrogen occurs at the interface between the anode and the electrolyte, shown in Fig. 2.

The energy conservation equation is expressed as Eq. (7), where k_{eff} is the effective thermal conductivity of the medium. For instance, in the porous electrodes the k_{eff} can be calculated by using Eq. (8), where the k_{fl} and k_s are the thermal conductivities of fluid and solid, and γ is the porosity of the porous medium.

$$\nabla\left(\vec{v}\left(\rho\sum_i Y_i h_i + p\right)\right) = \nabla\left(k_{\text{eff}}\nabla T + \sum_i h_i\left(\sum_{j=1}^{n-1}\rho D_{ij}\nabla Y_j\right)\right) + S_h \quad (7)$$

$$k_{\text{eff}} = \gamma k_{\text{fl}} + (1-\gamma)k_s \quad (8)$$

For the heat balance, the considered computational domain is a single repeated cell unit in the model and is assumed to be thermally isolated from all sides. The heat generated by the electrochemical reaction occurring in the reaction zone of the anode will be transferred into the electrodes, gas phase and interconnect by three ways: conduction, convection and radiation. Between the solid and the gas streams the heat is mainly exchanged by convection, while through porous or solid parts of the electrodes and interconnects the heat conduction is considered as the dominant way. In Eq. (7), the first and second terms on the right-hand side represent heat transfer due to conduction and gas species diffusion, respectively. The heat generated by electrochemical reaction is included in energy source S_h. While in the solid regions in the

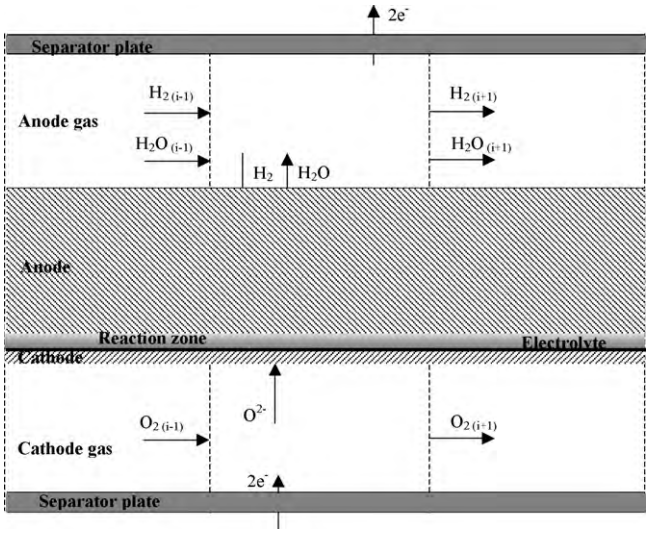

Fig. 2. Principles of mass transfer inside SOFC.

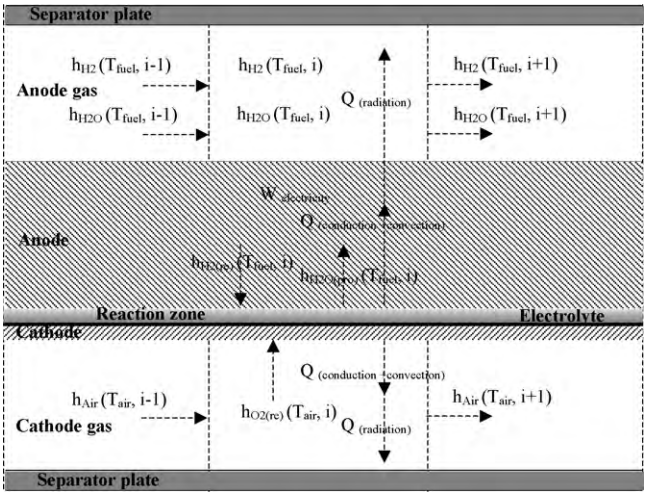

Fig. 3. Principles of electrochemical reaction and heat transfer.

model such as the interconnect the energy transport equation is simplified to the following form (9). And the convective heat transfer is represented as the first term of Eq. (9):

$$\nabla(\vec{v}\rho h) = \nabla(k\nabla T) + S_h \quad (9)$$

Besides the heat conduction and convection, due to the SOFC's high operating temperature the effect of radiative heat transfer is also evaluated in the study. For this purpose, the radiative heat transfer equation (RTE) is implemented to model the radiation heat transfer by using the discrete ordinates (DO) method. The DO radiation model solves the radiative transfer equation for a finite number of discrete solid angles, each associated with a vector direction $\vec{s}$ fixed in the global Cartesian system. The DO model treats the RTE in the direction $\vec{s}$ as a field equation. The radiative heat transfer equation for an absorbing, emitting, and scattering medium at position $\vec{r}$ in the direction $\vec{s}$ can be written as Eq. (10):

$$\frac{dI(\vec{r},\vec{s})}{ds} + (\alpha_r + \sigma_s)I(\vec{r},\vec{s}) = an^2\frac{\sigma T^4}{\pi} + \frac{\sigma_s}{4\pi}\int_0^{4\pi} I(\vec{r},\vec{s}')\Phi(\vec{s},\vec{s}')d\Omega' \quad (10)$$

However, due to the lack of sufficiently accurate properties of gases, for simplicity in this work it is assumed that the phenomena of absorption, of the participating gases in the fuel are ignored. Therefore, in the radiation heat transfer the gases are considered as transparent media and the absorption coefficient α_r is zero. Only the radiative heat exchange between gray walls (interconnects and PEN) are considered with emissivity of 0.9.

The rate of heat generation $\dot{Q}$ is determined from Eq. (11):

$$\dot{Q} = \frac{i}{nF}\Delta H_{\text{ECR}} - iV_{\text{cell}} \quad (11)$$

where $\dot{Q}$ stands for the heat generation rate; ΔH_{ECR} represents the enthalpy of the electrochemical reaction occurring at the reaction zone close to electrolyte inside anode; i is the current density at each point; n is the number of electrons transferred through the reaction; F is the Faraday constant; V_{cell} is the voltage of the cell. Figs. 2 and 3 represent the principles of mass transfer and heat transfer inside SOFC, respectively.

2.3. Electrochemical model

The electrochemical model calculates the local current density in the cell. In SOFCs, the oxidant, which is oxygen in the air in this

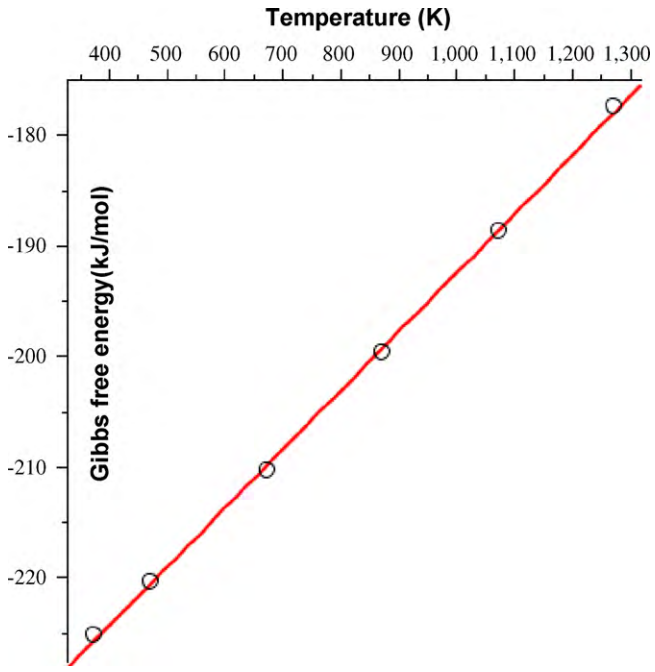

Fig. 4. Gibbs freee energy change for the H_2 oxidation reaction.

case, is fed into the cathode gas channel. At the cathode the oxidant reduction occurs, which can be expressed as Eq. (12):

$$\frac{1}{2}O_2 + 2e^- \rightarrow O^{2-} \tag{12}$$

The oxygen ions generated at the cathode pass through the electrolyte and then take part in the electrochemical reaction at the active reaction area of the anode, which in this model is the thin layer of the anode close to the electrolyte, as shown in Fig. 3. The electrochemical reaction of hydrogen with oxygen ions is represented in Eq. (13). The overall reaction is an exothermic process, shown in Eq. (14):

$$H_2 + O^{2-} \rightarrow H_2O + 2e^- \tag{13}$$

$$H_2 + \frac{1}{2}O_2 \rightarrow H_2O; \quad \Delta H_{298} = -241\,\mathrm{kJ\,mol^{-1}} \tag{14}$$

The cell voltage (V_{rev}) is locally changing with gas composition and temperature at the electrodes, and can be determined by the Nernst Eq. (15) for the electrochemical oxidation of hydrogen.

$$V_{rev} = V^0_{H_2} + \frac{RT}{2F}\ln\left(\frac{p_{H_2}{p_{O_2}}^{0.5}}{p_{H_2O}}\right) \tag{15}$$

where the p_{H_2}, p_{O_2}, p_{H_2O} and R represent the partial pressure of hydrogen, oxygen, water vapor and gas constant, respectively. $V^0_{H_2}$ stands for the standard potential for the hydrogen oxidation reaction at temperature T, and is the change of Gibbs free energy for the formation reaction of water divided by $2F$, as shown in Eq. (16) [1]. In this model the value of the Gibbs free energy is calculated using Eq. (17), deduced from experimental value shown in Fig. 4.

$$V^0_{H_2} = \frac{\Delta_f \bar{g}}{2F} \tag{16}$$

$$\Delta_f \bar{g} = 0.053T - 245.58 \tag{17}$$

The open-circuit potential (V_{rev}) is the maximum voltage which can be achieved by a fuel cell under specific operation conditions. However, the actual voltage of a real cell (V_{cell}), equal to the voltage difference between the cathode and the anode, is lower than V_{rev}. The difference between V_{rev} and V_{cell} is due to the internal resistances, electrode overpotential losses and contact resistances. In this work the resistance values used for the electrochemical reactions are values from the single cell measurements in alumina housings using Pt and Ni grids and the resistance of the contact coatings are not included in the equation. The resistance values for these coatings were not determined in the current work and it is assumed that this will not be important for stack behaviors. An empirical formula Eq. (19) was derived for estimating the value of the total local losses ($R_{tot.loc}$) occurring in the operating cell, which is a function of temperature T, where k_0, E_a and R are constants, summarized in Table 1. Therefore, the operating cell voltage (V_{cell}) can be expressed as Eq. (18):

$$V_{cell} = V_{rev} - iR_{tot.loc} \tag{18}$$

Since the anode and metal parts in the stack are good conductors, a constant cell voltage of 0.8 V is assumed in this work. All the losses are in part responsible for the heat generated in an operating fuel cell and will be explained later.

$$R_{tot.loc} = k_0 \exp\left(\frac{-E_a}{RT}\right) \tag{19}$$

The derived empirical formula of total resistance in the cell is valid in the temperature range between 950 and 1073 K. Finally the current density is calculated by Eq. (20):

$$i = \frac{V_{rev} - V_{cell}}{R_{tot.loc}} \tag{20}$$

In order to better explain the method for the electrochemical reaction model, the whole single cell unit can be treated as a number of small sub-cells or elements in series in Figs. 2 and 3. In each element, the electrochemical reaction rates are calculated based on the inlet boundary conditions (species concentrations, temperatures, etc.) resulting from the previous element. For the first sub-cell in the calculation, the initial inlet boundary condition is assigned. By this way, the local electrochemical parameters will be known for each element in the whole domain. According to Faraday's law, the rates of the electrochemical reactions depend on the current density i [11,12],

$$i = 2F\frac{dH_2}{dt} = 4F\frac{dO_2}{dt} \tag{21}$$

where the dH_2/dt and dO_2/dt are the molar consumption rates of the hydrogen and oxygen at the anode and cathode, respectively. Therefore, in this element the number of moles of hydrogen and oxygen consumed and water produced can be calculated by Eq. (22):

$$i = 2Fn^{reac}_{H_2} = 4Fn^{reac}_{O_2} = 2Fn^{reac}_{H_2O} \tag{22}$$

This relation relies on the fact that the electrolyte in SOFCs, such as YSZ, are pure ionic conductors, and therefore only oxygen ions can permeate through the electrolyte to participate in the oxidation reaction at the anode/electrolyte interface.

3. Results and discussion

The Navier–Stokes and transport equations are solved in each grid of the model by the finite volume method using a commercial computational fluid dynamics simulation code, Fluent, coupled with the user-defined electrochemical reaction model to investigate the operating parameters of the proposed SOFC. In the calculation, the information of gas species concentrations and temperatures at the local points in the cell unit obtained from the thermal fluid model is passed to the electrochemical model to calculate the local current density, which is utilized for the calculation of the hydrogen and oxygen reaction rate, species sources and heat generated in the cell. And then the updated information

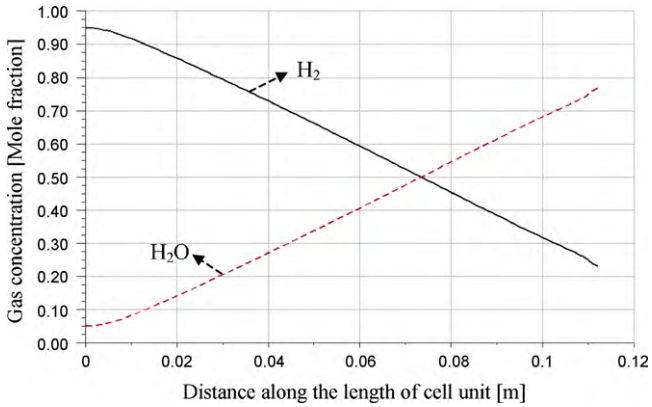

Fig. 5. Gas species concentration in the anode gas channel along the length of the cell.

of species concentrations and temperature distribution will be calculated again for the next iteration, and so on, until convergence of the solution is achieved. The current modeling work concerns with the study of two cases, which are the basic case with inclusion of the conduction and convection heat transfer, and the second case with the additional effect of radiative heat transfer considered. For simplicity, here the basic case is defined as case I and the second case as case II.

In this section, the model results for the gas species concentration and current density profiles along the length of the cell will be discussed first for the case without considering radiative heat transfer. Then the temperature distributions at different locations within the cell along the length will be given for both cases with and without radiation. Finally the effect of radiation heat transfer will be evaluated by comparison of temperature profiles of the two cases.

3.1. Gas species concentration

Mole fraction profiles of the reactant and product gas species in the anode gas channel along the length of the cell are shown in Fig. 5. Due to the electrochemical reaction between the hydrogen in the fuel fed from inlet and oxygen ions from cathode side passed through the electrolyte, the concentration of hydrogen in the anode gas channel keeps dropping from the maximum of 95% at the inlet to the lowest point at the outlet with the consumption of hydrogen along the flow direction. Meanwhile, the concentration of the product gas, water vapor, shows an increase along the length of the cell unit, correspondingly. At the exit of the fuel channel, the average concentration of hydrogen in the gas stream is 19% with a fuel utilization of 0.8.

The hydrogen mole fraction distribution on the middle vertical cross-section of the anode gas channel is shown in Fig. 6. The enlarged part in Fig. 6 shows the hydrogen concentration distribution in the vertical direction of the cross-section. In the model, it is assumed that the electrochemical reaction occurs at the interface (reaction zone) between the anode and electrolyte, where hydrogen is consumed and reacted. Therefore, in Fig. 6, along the vertical direction from the cathode and electrolyte to the top of the fuel channel the mole fraction of hydrogen shows an increasing trend. The difference of the concentration of the hydrogen in the vertical direction makes the hydrogen diffuse to the reaction site from fuel gas channel through the porous anode substrate.

3.2. Current density profile

The predicted current density profile, Nernst voltage and resistance ($R_{tot.loc}$) along the cell length are shown in Fig. 7. Under

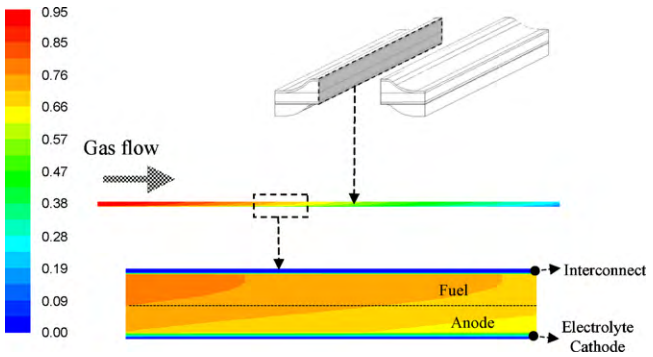

Fig. 6. Hydrogen concentration on the middle cross-section of anode gas channel.

the proposed operating conditions the current density varies in the range from 5100 to 7900 A m^{-2} and keeps rather steady along most of the length of the cell except for the ending region, with an average current density of 7276 A m^{-2}. At the beginning part, the current density profile keeps flat till the length of 10 mm. Afterwards, the current density steadily rises to the peak value of 7900 A m^{-2} at 62 mm along the cell length. For the final 50 mm of the cell length a severe drop of the current density is observed. As Eq. (16) expressed, the current density depends on several factors and operating parameters implemented into the model, e.g. the concentrations of gas species, the temperature and the cell operating voltage, etc. In this work, the inlet temperature of gases is assumed to be 973 K and the cell voltage is 0.8 V. In Fig. 7, the Nernst voltage and cell resistance are both declining along the length of cell. However, in the beginning part the rate of decrease of Nernst voltage is slower than the rate of decrease of the resistance. At a certain point which is around the location where the highest current density appears, the decrease of resistance becomes slower than the Nernst voltage. The combination of both cell resistance and Nernst voltage results in the convex curve of the current density shown in Fig. 7.The difference between the Nernst voltage and the cell voltage decreases rather fast from inlet to outlet, by which the driving force for the current at the outlet is low resulting in a decrease in current density near the outlet of the cell.

3.3. Temperature distribution

In this section, the temperature profiles for the locations of the interconnect, PEN structure and bottom of cathode gas channel

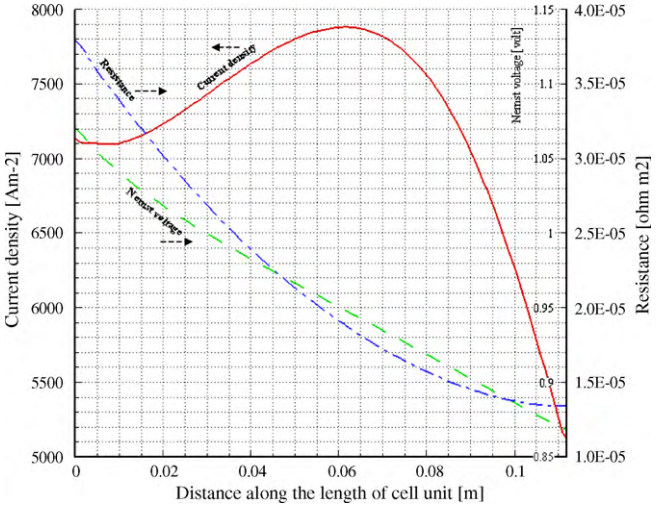

Fig. 7. Current density, Nernst voltage and resistance along the length of the cell unit.

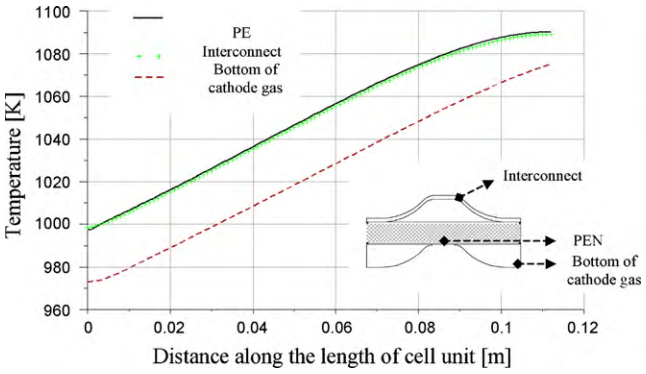

Fig. 8. Temperature profiles of interconnect, cell and bottom of the cathode gas channel along the length of cell without radiation heat transfer.

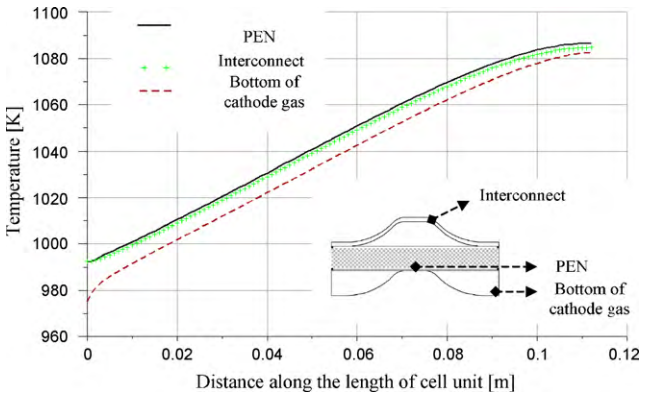

Fig. 9. Temperature profiles of interconnect, cell and bottom of the cathode gas channel along the length of cell with radiation heat transfer.

along the cell length and temperature distributions on the cross-sections in the model are presented for both case I and case II. In this work, the temperature gradient over the stack is set to be around 100 °C. In order to maintain this gradient at a certain power level a certain amount of air is needed. Therefore a ratio of air to fuel is set as 10 here to make sure the designed temperature difference in the channel.

The temperature profiles of case I are shown in Fig. 8. The electrochemical reaction takes place in the reaction zone, close to the electrolyte, inside which the reaction heat is generated. Therefore the temperature at the interface between the anode and electrolyte is the highest. Due to the good thermal conductivity of the whole PEN structure (cell part) the heat is uniformly distributed within the PEN and, the temperature of the reaction zone inside the anode here stands for the whole PEN structure. And PEN structure is the location with the highest temperature in Fig. 8. The temperature profile of the interconnect is identical to that of PEN, which can be explained by the fact that in the proposed design the interconnect has a good connection with the PEN structure and thus the heat can be conducted rapidly. Because the interconnect is solid metal with a high thermal conductivity the temperature is uniform inside the interconnect.

As the cathode gas serves as both the coolant and oxydant, the temperature of the bottom of the cathode gas channel, in Fig. 8, is the lowest for case I under the assumption that the single cell unit is thermally isolated from the surroundings. The temperature difference between the PEN (location with the highest temperature) and the bottom of the cathode gas channel (location with the lowest temperature) is in the range of 20–26 K. On the other hand, through the length of the cell unit the temperature keeps increasing from inlet to outlet due to the exothermic electrochemical reaction. The inlet temperature of the interconnect and PEN structure is 997 K and the outlet is 1090 K. Therefore, approximately 93 K of temperature rise takes place between the inlet and outlet. Meanwhile, the temperature of the bottom of the cathode gas channel

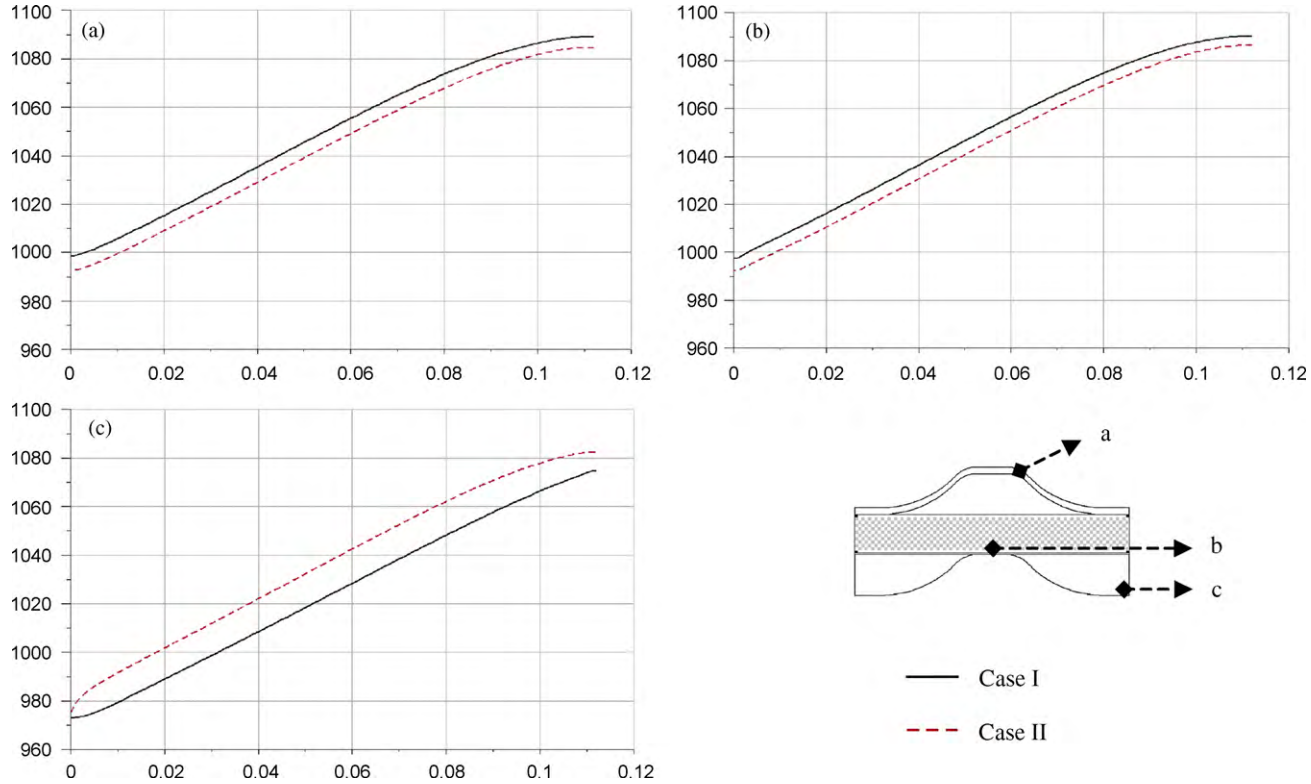

Fig. 10. Comparison of the temperature profiles of the interconnect (a), cell (b) and bottom of cathode gas channel (c) for both cases.

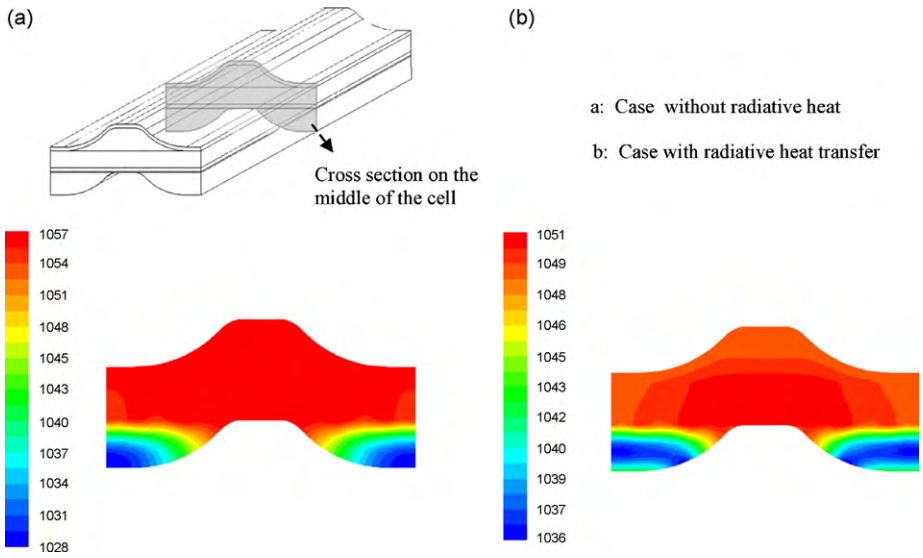

Fig. 11. Temperature distributions on the cross-section of cell unit for both cases [K].

increases from 973 K at the inlet to 1075 K at the outlet, and 102 K of temperature difference is seen.

The temperature profiles of the corresponding locations for case II are illustrated in Fig. 9. Similarly an increasing trend of the temperature along the cell length is present. However, with the heat transfer due to radiation considered, the temperature difference between the PEN and the bottom of the cathode gas channel is much less than for case I. For most parts of the cell length the temperature of the PEN is only 11 K higher than the temperature of the bottom of cathode gas channel. Unlike the same temperature profile between the PEN and interconnect in case I, in Fig. 9 the temperature of interconnect is 1–2 K lower than the PEN. The temperature increase of the PEN is 96 K (from 993 to 1086 K) and that of the cathode gas bottom is 95 K (from 973 to 1082 K). Therefore, in case II the temperature increases less from the inlet to outlet than in case I.

In order to clearly observe the difference in temperature profiles for both cases and analyze the effect of heat radiation, Fig. 10 shows the comparisons of the temperature profiles at the different locations in the cell unit for case I and case II. Fig. 10a is the comparison of interconnects; Fig. 10b is the PEN structure; Fig. 10c is the bottom of the cathode gas channel. In Fig. 10a and b it can be found that the temperatures of the interconnect and PEN for case II are 7–8 K lower than for case I at the corresponding cell length. However, on the cathode gas side, the temperature of the bottom of the cathode gas channel is 12–13 K higher for case II. Apparently, the heat transfer enhancement by the thermal radiation decreases the temperature differences in the whole cell unit.

The temperature profiles of the different locations in the cell unit mentioned above show the temperature differences along the cell length. However, the details of temperature variation on the cross-sections of the cell unit cannot be seen from the general trends of temperature profile. Only with the detailed temperature field on the cross-sections the effect of radiation heat transfer on the temperature distribution could be correctly evaluated and explained. Fig. 11 demonstrates the temperature distribution on the cross-section of the cell unit, for both cases. Fig. 11a is case I and Fig. 11b is case II. In Fig. 11a the temperature of case I varies between 1028 and 1057 K and a difference of 29 K across-the section is observed. In the region of the interconnect, the PEN structure, and fuel gas, the temperature is higher and comparatively evenly distributed. Across-the cathode gas channel from top to bottom the temperature decreases dramatically with the minimum temperature appearing at the bottom of the cathode gas channel. Nevertheless, in case II, as illustrated in Fig. 11b, the temperature is changing between 1036 and 1051 K with the temperature difference of only 15 K. Compared with case I, the variation of temperature of case II is much less. In this study, the absorption of the gas medium was not considered. The heat produced by electrochemical reaction in the reaction zone will be transferred to the interconnect and the bottom solid wall of the cathode gas channel by thermal radiation besides conduction and convection. In Fig. 11b the temperature distribution is different from case I especially on the region of the cathode gas channel. The temperature of the bottom of the cathode gas channel is higher than the center of the cathode gas in case II because the radiation effect. Therefore, for case II the center of the cathode gas channel is the location with the lowest temperature. Due to the lower temperature difference in case II it can be deduced that considering radiation heat transfer can result in a more uniformly distributed temperature in the single repeated cell unit, and furthermore thermal radiation can also lead to more moderate temperature gradients in the cell unit.

Figs. 12 and 13 illustrate the temperature variation on the cross-section of anode gas channel (A–A) and cathode gas channel (B–B) along the cell length for case I and case II, respectively. In order

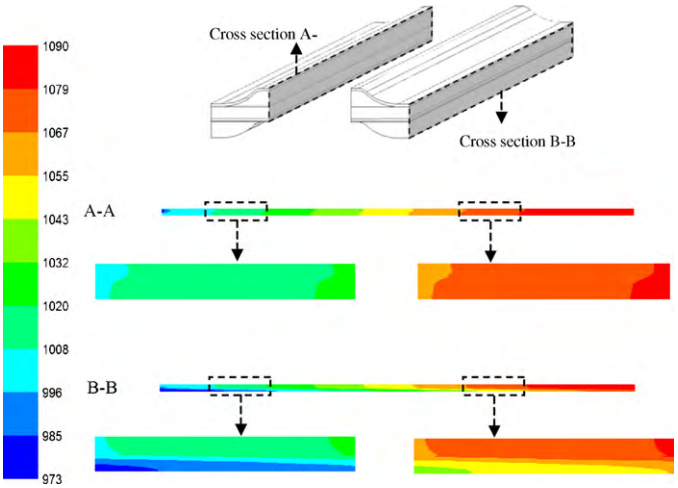

Fig. 12. Temperature distributions on the cross-sections of anode gas channel and cathode gas channel in the cell unit for case I.

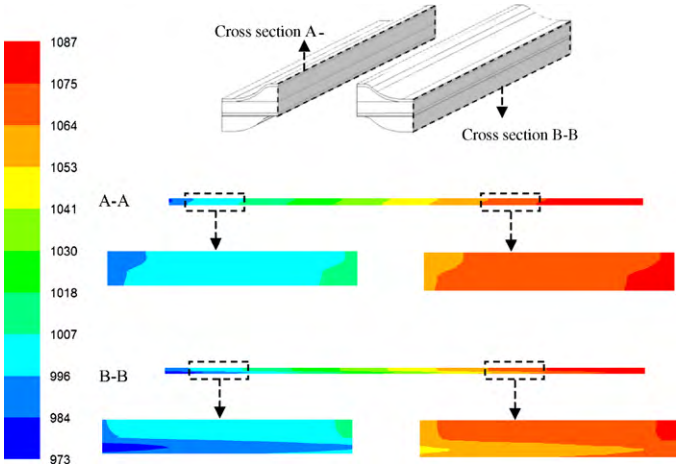

Fig. 13. Temperature distributions on the cross-section of anode gas channel and cathode gas channel in the cell unit for case II.

to clearly show the temperature field, the enlarged pictures are presented, giving the details of the temperature field for different positions in the figures. The results show that radiation has a significant effect on the temperature fields in the cell, especially for the cathode gas channel. Due to the inclusion of the heat radiation, a lower temperature change is observed in case II and thus the thermal stress could be less, which could minimize the probability of thermally incurred failure. Therefore, it can be concluded that for evaluating the temperature distribution of a single unit cell the effect of radiative heat transfer should be considered.

4. Conclusions

A three-dimensional anode-supported intermediate-temperature planar SOFC unit model including anode, cathode, electrolyte, fuel, air and an interconnect incorporating electrochemical reactions has been developed. The developed model can be used as a tool to investigate the thermal, fluid dynamic and electrochemical behaviors of the proposed SOFC design operating at given conditions. The SOFC system with a co-flow design studied in this work is with inlet fuel and air temperatures of 973 K and 80% fuel utilization operated at an output voltage of 0.8 V. Detailed results from the studies have been reported. The reaction regions modeled in this work are distinguished in the SOFC instead of simply assuming surface reactions or solid reactions in the PEN. The model results were calculated based on the proposed cell design, but is also applicable for the analysis of other designs. Modeling results of the gas species concentrations, the current density distribution and the temperature profiles along the cell length and the cross-sections of the cell unit are obtained. Especially the effect of the thermal radiation on the temperature distribution was evaluated by the comparison of two cases. Based on the modeling results and analysis, it can be concluded that a relatively uniform current density distribution was achieved for the proposed design at the given operating conditions with the average value of approximately 5800 A m^{-2} over the active area of the cell. Additionally, the radiation effects are important on the accurate prediction of temperature field for the single repeated fuel cell unit. Neglecting the radiation in the model will result in an incorrect temperature distribution, and thus misleads the calculation of temperature gradients and other properties and parameters in the single cell unit. Therefore, for modeling and accurate prediction of temperature field in the single SOFC unit with the assumption of the adiabatic top and bottom external boundaries, the inclusion of radiative heat transfer is necessary. However, radiation phenomena are rather complicated, and the current work will not go to the details of the radiation. In future, the model could be further improved by incorporating the effects of these participating media. A model with multiple cells connected in series is developed for the study considering the heat transfer from one single cell unit to another.

Acknowledgement

This work was supported by SenterNovem (EOS-LT project).

References

[1] S.C. Singhal, K. Kendall (Eds.), High Temperature Solid Oxide Fuel Cells: Fundamentals, Design and Applications, 1st ed., Elsevier Ltd., Oxford, UK, 2003.
[2] U.S. DOE, Fuel Cell Handbook, 7th ed., National Energy Technology Laboratory, 2004 (November).
[3] S. Kakaça, A. Pramuanjaroenkijb, X.Y. Zhou, A review of numerical modeling of solid oxide fuel cells, Int. J. Hydrogen Energy 32 (2007) 761–786.
[4] K. Nikooyeh, A.A. Jeje, J.M. Hill, 3D modeling of anode-supported planar SOFC with internal reforming of methane, J. Power Sources 171 (2007) 601–609.
[5] J.D.J. VanderSteen, J.G. Pharoah, Modeling Radiation Heat Transfer With Participating Media in Solid Oxide Fuel Cells, J. Fuel Cell Sci. Technol. 3 (2006) 62–67.
[6] D. Cui, M. Cheng, Numerical analysis of thermal and electrochemical phenomena for anode supported microtubular SOFC, AIChE J. 55 (3) (2009) 771–781.
[7] G. Wang, Y. Yang, H. Zhang b, W. Xia, 3-D model of thermo-fluid and electrochemical for planar SOFC, J. Power Sources 167 (2007) 398–405.
[8] S. Murthy, A.G. Fedorov, Radiation heat transfer analysis of the monolith type solid oxide fuel cell, J. Power Sources 124 (2003) 453–458.
[9] K.J. Daun, S.B. Beale, F. Liu, G.J. Smallwood, Radiation heat transfer in planar SOFC electrolytes, J. Power Sources 157 (2006) 302–310.
[10] Qiang Hu, Shaorong Wang, Ting-Lian Wen, Analysis of processes in planar solid oxide fuel cells, Solid State Ionics 179 (2008) 1579–1587.
[11] H. Yakabe, T. Ogiwara, M. Hishinuma, I. Yasuda, 3-D model calculation for planar SOFC, J. Power Sources 102 (2001) 144–154.
[12] S. Campanari, P. Iora, Definition and sensitivity analysis of a finite volume SOFC model for a tubular cell geometry, J. Power Sources 132 (2004) 113–126.
[13] D. Sánchez, R. Chacartegui, A. Muñoz, T. Sánchez, Thermal and electrochemical model of internal reforming solid oxide fuel cells with tubular geometry, J. Power Sources 160 (2006) 1074–1087.
[14] P. Costamagna, A. Selimovic, M. Del Borghi, G. Agnewc, Electrochemical model of the integrated planar solid oxide fuel cell (IP-SOFC), Chem. Eng. J. 102 (2004) 61–69.
[15] P. Aguiara, C.S. Adjiman, N.P. Brandon, Anode-supported intermediate temperature direct internal reforming solid oxide fuel cell. I: model-based steady-state performance, J. Power Sources 138 (2004) 120–136.
[16] B. Todd, J.B. Young, Thermodynamic and transport properties of gases for use in solid oxide fuel cell modeling, J. Power Sources 110 (2002) 186–200.
[17] B.E. Poling, J.M. Prausnitz, J.P. O'Connell, The Properties of Liquids & Gas, 5th ed., McGraw-Hill, New York, 2000.